Article | Received 8 February 2024; Accepted 10 May 2024; Published 13 June 2024
https://doi.org/10.55092/am20240007

Computational design for injection continuous liquid interface production

Gabriel Lipkowitz[1], Navneeth Krishna[1], Ian Coates[2], Eric Shaqfeh[1,2,*], Joseph DeSimone[2,3,*]

[1] Department of Mechanical Engineering, Stanford University, Stanford, CA 94305, USA
[2] Department of Chemical Engineering, Stanford University, Stanford, CA 94305, USA
[3] Department of Radiology, Stanford University, Stanford, CA 94305, USA

* Correspondence authors; E-mails: esgs@stanford.edu; jmdesimone@stanford.edu.

Abstract: While resin 3D printing allows designers to fabricate complex 3D objects, the technology has not found widespread adoption in manufacturing as a result of slow print speeds, poor reliability, and cumbersome support structures. The last of these in particular waste material, require human labor, are tedious to remove, and damage surface finish, but are fundamentally necessary due to adhesion forces and a lack of control of fluid flow during the printing process. Current design for additive manufacturing (DfAM) industry standards do not seek to offset such forces; instead, they empirically call for reducing printing speeds and/or imposing cumbersome supporting structures. Injection continuous liquid interface production (iCLIP) is a recent approach capable of effectively nullifying such forces by injecting resin into the deadzone. The method has been demonstrated to date for the case of a single channel running through an object formed of rigid material. However, the possibility of innervating the growing object with multiple channels – engineered into the CAD design uniquely for every print by this fabrication approach – remains unexplored. In this work we described our computational modeling and design approach to accompany iCLIP, optimally innervating the part with channels to infuse resin into the deadzone. We detail our modeling approach for both single and multiple injection sites, and for Newtonian and non-Newtonian resins. After describing our hardware implementation to evaluate our approach, we provide experimental validation of our simulation-driven injection scheme, including using both rigid and elastomeric resins. We demonstrate such a DfAM approach can significantly increase print speed and reduce the need for supports in a user's 3D model. In doing so, our approach promises to enhance the scalability of resin 3D printing and to hasten its adoption in real-world manufacturing settings.

Keywords: Generative design, additive manufacturing, 3D printing

1. Introduction

3D printing allows designers to realize intricate computer-aided design (CAD) models at high resolution, and with increasingly broad libraries of materials. Beyond extrusion printers primarily utilized for prototyping, resin 3D printing has begun to experience adoption in real-world manufacturing [1], thanks to its capacity to fabricate objects with exceptionally smooth surface finish and isotropic material

properties, with heterogeneous lattice geometries, and, finally, with elastomers for high energy absorption or return. Emerging applications include wearable sensors [2], haptic interfaces [3], architected metamaterials [4], and medical implants [5], among others [6].

However, significant bottlenecks remain that prevent the more widespread adoption of resin 3D printing in real-world manufacturing and fabrication settings. First is the relatively low speed, with typical stereolithography (SLA) and digital light projection (DLP)-based printers requiring hours to days to fabricate objects. In traditional SLA and DLP printing, objects solidify to the window at every slice and must be forcibly detached, which exerts significant stresses on the elevating part and limits speeds in these systems. SLA and DLP technologies have explored multiple methods to lessen these separation forces, thus aiming to enhance printing speed. Mainstream commercial printers based on SLA and DLP often combine lift, retract, and at times, slide actions to ensure the printed part detaches from the window smoothly. Other fabrication strategies include utilizing vibration techniques [7], adjusting the vat's orientation with each layer to manage resin distribution [8], modifying the tension of the vat film [9], and employing hydraulic techniques for active separation [10]. Recently, continuous liquid interface production (CLIP) has significantly accelerated printing by maintaining a thin liquid interface, the deadzone, between the growing part and the window, obviating the lift-and-retract mechanism of SLA and DLP-based printers [11]. However, due to the very thin deadzone, CLIP is still speed-limited because of the separation forces arising from pulling the part upwards from the projection window. If uncontrolled, these forces cause print failure, limiting both speed and part area: specifically, if these forces exceed the work of adhesion between the part's initial layer and the typically metal build platform, separation of the growing part from the platform occurs, *i.e.* adhesive failure. These forces can also cause delamination of subsequent layers and newly cured layers, *i.e.* cohesive failure. Such suction forces can also cause observable layering, stair-stepping, and cavitation defects if the negative pressure within the deadzone grows too large [12]. These forces ultimately are the rate-determining step in the speed of these processes, as it is well-known that the photopolymerization reaction itself is nearly instantaneous. Such forces have important practical consequences for CLIP-based printing. As shown when first introduced, CLIP can accelerate printing by orders of magnitude when carried out in a fully continuous manner [13, 14]. However, in reality this is often not the case, due to the aforementioned adhesion forces; instead, printer kinematics are not fully continuous, but often executed in discontinuous motions, be they stepped or pumped, both in industry and in academic settings [15, 16]. This means CLIP is still too slow to compete with injection molding in many applications. In commercial printer software, print parameters are often tuned empirically using trial-and-error expertise and trade knowledge of field engineers, whereby user-observed errors prompt unique, custom changes in print parameters. By contrast, in this work we propose a simulation-driven design approach for iCLIP-based 3D printing that seeks to offset suction forces directly.

A second major limitation on the scalability of vat polymerization are supports. In the conventional CLIP process depicted in Figure 1, supports play a crucial role in linking the evolving structure to the building surface. For the majority of 3D printing tasks, these supports are indispensable, introduced between the design and printing phases to counteract forces that might otherwise hinder successful printing. They become particularly vital for features that extend horizontally—termed "overhanging" features—especially in areas that lack preceding layers for firm solidification. The absence of such supports in a design can lead to common issues like drooping, warping, or layer misalignment during

traditional 3D printing. While supports mitigate these problems, they introduce a set of challenges. For newcomers to 3D printing, determining which parts of their design need supports can be perplexing, and this might vary depending on the chosen material. Although tools that automatically generate support structures are available, they might not align with the designer's intent, necessitating extensive manual adjustments. Such tools primarily rely on geometric guidelines, leading to occasional failures in defect prevention. More advanced tools that use finite element analysis (FEA) for support generation are available [17], but they demand substantial computational resources and time. Moreover, the post-printing phase demands considerable manual intervention to remove these supports, which often mars the object's surface finish. In extrusion-based printing, supports are typically dissolvable or recyclable [18]. However, for resin-based 3D printing, supports are usually waste, which is environmentally unsustainable. Many support-minimization algorithms exist for fused deposition modeling, including thin support shell enclosures [19], long-spanning bridge structures [20], branch-merging mechanisms [21], and slender tree-like structures [22], but these do not necessarily aid in resin printing, where suction forces are often orders of magnitude larger than gravity. The work described in this paper is motivated by the lack of suitable methods to reduce supports during resin printing specifically.

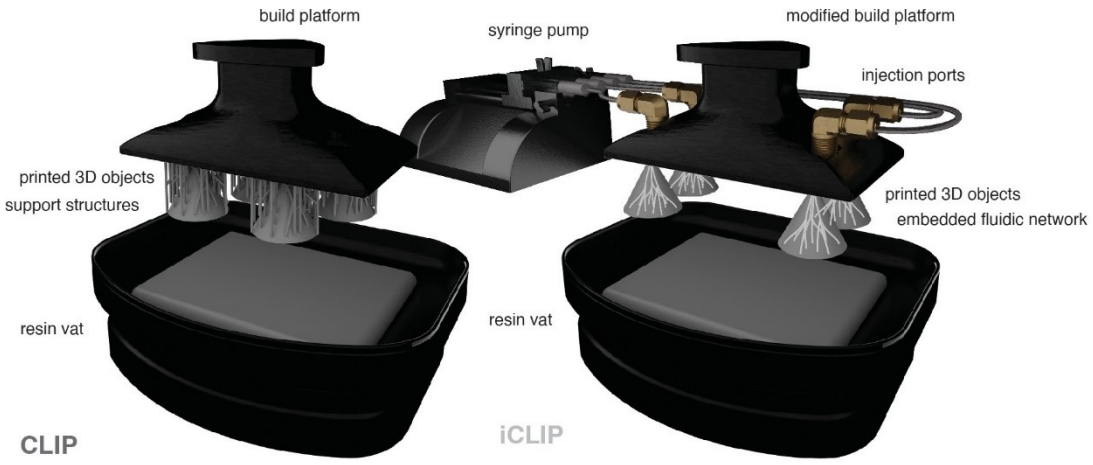

Figure 1. Schematic illustration of CLIP printing without injection, and with support scaffolding to offset suction forces, and injection CLIP printing with a co-designed fluidic network through which resin is introduced from an external supply.

The inherent compliance of flexible materials in the green state during printing also renders them the most difficult to print due to the aforementioned suction forces. Thus, printing these flexible materials requires the most print time, necessitates the highest amount of support material, causes more failures in practice than rigid materials, and imposes the most severe overhang feature restrictions [23]. At times it is entirely infeasible to remove supports from such objects post-printing since they are fragile and tear easily. Nonetheless, emerging soft materials represent an area of high interest to the 3D printing community for fabricating interactive objects, ranging from wearables [24] to augmented reality devices [25]. These include printable elastomers [26] and less traditional, but still printable, flexible materials [27, 28]. Combining such materials with lattice architectures achievable only with 3D printing enables

even more complex applications, including for e.g. haptic gloves [29]. and products with embedded capacitive touch sensing [30]. More efficient platforms for processing these materials to achieve emerging applications are therefore imperative, but an inability to control and direct fluid flows during vat 3D printing has made progress slow to date.

Injection continuous liquid interface production

Injection continuous liquid interface production (iCLIP) incorporates resin flow through fluidic pathways directly embedded within the 3D structure, acting as an enhancement to the CLIP system [31]. This setup, as illustrated schematically in Figure 1, facilitates resin flow navigating from the platform, through the embedded channels, reaching the deadzone during the printing phase. These inbuilt channels can later be solidified using a thermal post-cure process, a common practice in commercial 3D printing. In its introduction [31], iCLIP demonstrated the capability of single injection through an embedded channel to effectively neutralize suction forces, but the potential benefits of incorporating multiple channels for offsetting suction, however, have not been simulated and experimentally demonstrated heretofore, and neither has the potential impact on printing with elastomeric resins or on printing with complex geometries with variable overhang features. In this work, we consider the quantitative degree to which injection rate, along with the number of injection channels, affects such print reliability metrics in the iCLIP manufacturing process. This multiple channel co-design, and its impact on deadzone pressure profiles, especially as applied to elastomeric resins with non-Newtonian rheology, is the subject of this paper. In this work, we detail our simulation strategy for both single and multiple injection sites and for Newtonian and non-Newtonian resins. After describing our hardware implementation to assess our simulations, we provide experimental validation, including printing with elastomeric resins. In this work, we model and demonstrate that innervating a network into the part can extend the maximum achievable unsupported overhang angle, for both rigid and elastomeric materials, by 15 ± 5 degrees, and can increase print speeds for overhang geometries by up to two-fold without defect.

2. Computational modeling of iCLIP 3D printing

Lubrication theory provides approximates well fluid flows in gaps where characteristic horizontal length scales greatly exceed vertical length scales. We non-dimensionalize such that $\tilde{x} = \frac{x}{L}$, $\tilde{y} = \frac{y}{L}$, $\tilde{z} = \frac{z}{h}$, $\tilde{u}_z = \frac{u_z}{U}$, $\tilde{\vec{u}} = \frac{\tilde{u}\epsilon}{U}$, where z is the gap coordinate, ∇ the gradient operator in the $x-y$ plane, $\vec{u} = [u_x, u_y]$ the planar flow velocity, h the characteristic deadzone thickness, L the characteristic part dimension, U the print speed, μ the resin viscosity, and $\epsilon = \frac{h}{L}$. For resins which are Newtonian, the pressure field in a lubrication flow is governed by Poisson's equation in two dimensions x and y.

$$\tilde{\nabla}^2 \tilde{p} = 12\, u_z \ (\tilde{z} = 1) \tag{1}$$

Integrated over the footprint of the part gives us an approximation of the force F_S required to offset the suction forces. For a cylindrical part of radius R and $u_z\ (\tilde{z} = 1) = 1$:

$$F_s = -\frac{3\pi\mu U R^4}{h^3} \tag{2}$$

This is the famous Stefan adhesion force [32]. Detailed derivation of flow for Newtonian resins within the deadzone has been developed in prior work [31], and is summarized in brief in the Supplemental Information.

Flow for non-Newtonian resins is derived below and is relevant to this work that considers elastomeric resins that display such rheological properties (Figure S2). For Non-Newtonian resins, we use a power-law viscosity model (assuming cylindrical footprint):

$$\tau_{rz} = u_0 \left|\frac{\partial u_r}{\partial_z}\right|^{-n} \left(\frac{\partial u_r}{\partial_z}\right) \tag{3}$$

where μ_0 is the fluid viscosity parameter and n is the power-law index. We use the power-law viscosity model over other potential models for non-Newtonian resins because it effectively captures our experimental data as obtained from rheological characterization, as shown in Figure S2.

When $\epsilon \ll 1$, the governing momentum equations are $\frac{\partial_p}{\partial_z} \approx 0$ and $\tau_{rz} = \frac{\partial_p}{\partial_r}\left(z - \frac{h}{2}\right)$, and from continuity $\frac{1}{r}\frac{\partial}{\partial_r}\left(ru_r\right) + \frac{\partial_{u_z}}{\partial_z} = 0$. For a circular area of radius R, we solve for the flow field using the no-slip boundary condition for velocity at $z = 0, h$ and the homogeneous pressure boundary condition at $r = R$. Integrating the pressure field over the footprint of the part yields a revised force required to offset the suction forces when printing with a non-Newtonian resin at a print speed U:

$$F_s = -\frac{\pi\mu_0}{4-n}\left(\frac{U}{2\alpha(n)}\right)^{1-n} R^{4-n} \tag{4}$$

where $\alpha(n) = 2\left(\frac{1-n}{3-2n}\right)\left(\frac{h}{2}\right)^{\frac{3-2n}{1-n}}$ as compared to $F_s = -\frac{3\pi\mu UR^4}{2}$ for a Newtonian resin. Details of the full derivation can be found in our previous work [16]. The non-Newtonian resin in our study is characterized by $n = 0.4$ based on a power-law fit to the aforementioned EPU 40 resin rheological measurements.

For a Newtonian fluid, we modify the right-hand side of Equation 1 to account for injection with a forcing term, $f\ (x, y)$, at discrete locations in the fluid domain, whose magnitude depends upon the injection velocity relative to the print speed U, $\frac{\partial^2\tilde{p}}{\partial x^2} + \frac{\partial^2\tilde{p}}{\partial y^2} = 12\big(1 - f(x,y)\big)$ Mathematically modeling the injection as a point source and solving for the pressure field, the incremental pressure increase from injection becomes:

$$\tilde{p}_{injection}(r) \propto 6\tilde{Q}\ln\frac{1}{\tilde{r}} \tag{5}$$

where $\tilde{r}$ is the distance from the injection site non-dimensionalized with the part radius R, $\tilde{Q}$ the volumetric injection rate made dimensionless with the volumetric growth rate of the part πUR^2. When injecting material during printing at a dimensionless volumetric flow rate $\tilde{Q}$, the pressure increment is highest near the injection site and decays with distance. Overall, this means that the suction force F_S can be offset, provided a sufficient injection rate $\tilde{Q}$ is administered:

$$F_{inject} = 3\pi\tilde{Q}\frac{\mu UR^4}{h^3} \tag{6}$$

For a Newtonian fluid and multiple injection channels, the pressure profile with injection results from solving the partial differential equation:

$$\frac{1}{\tilde{r}}\frac{\partial}{\partial\tilde{r}}\tilde{r}\frac{\partial\tilde{p}^{(2)}}{\partial\tilde{r}}+\frac{1}{\tilde{r}^2}\frac{\partial^2\tilde{p}^{(2)}}{\partial\tilde{\theta}^2}=-12Q(\tilde{r},\theta) \quad (7)$$

where we again assume the footprint to be cylindrical. To obtain a tractable analytical form of the solution, the injection is assumed to be comprised of point sources at positions $(\tilde{r}_l', \tilde{\theta}_l')$ modeled mathematically as Dirac delta functions:

$$Q(\tilde{r},\theta)=\tilde{Q}\frac{\delta(\tilde{r}-\tilde{r}_l')\delta(\theta-\theta_l')}{\tilde{r}} \quad (8)$$

where $\tilde{Q}$ is the dimensionless volumetric flow rate through each injection channel. The resulting pressure field can be written as an expansion in Fourier-Bessel series for an L number of injection channels:

$$\tilde{p}^{(2)}\{\tilde{r},\theta\}=\sum_{n=0}^{\infty}\sum_{m=1}^{\infty}\sum_{l=1}^{L}\left\{\frac{12}{\lambda_{nm}^2}C_{nml}J_n(\lambda_{nm}\tilde{r})\cos n\theta+\frac{12}{\lambda_{nm}^2}D_{nml}J_n(\lambda_{nm}\tilde{r})\sin n\theta\right\} \quad (9)$$

with eigenvalues λ_{nm} corresponding to $J_n(\lambda_{nm})=0$, and where:

$$C_{nml}=\begin{cases}\frac{2\tilde{Q}_l}{J_{n+1}^2(\lambda_{nm})}J_n(\lambda_{nm}\tilde{r}_l')\cos n\theta_l', & n\neq 0\\ \frac{\tilde{Q}_l}{J_1^2(\lambda_{0m})}J_0(\lambda_{0m}\tilde{r}_l'), & n=0\end{cases} \quad (10)$$

$$D_{nm}=\frac{2\tilde{Q}_l}{J_{n+1}^2(\lambda_{nm})}J_n(\lambda_{nm}\tilde{r}_l')\sin n\theta_l' \quad (11)$$

The Stefan force due to injection is obtained by integrating the pressure field including the sources. For printing with a Newtonian resin, we obtain a net Stefan force due to suction and injection as:

$$F_{Stefen}=\left\{-\frac{3\pi}{2}+24\pi\sum_{l=1}^{L}\tilde{Q}_l\sum_{m=1}^{\infty}\frac{J_0(\lambda_{0m}\tilde{r}_l')}{\lambda_{0m}^3J_1(\lambda_{0m})}\right\}\frac{\mu UR^4}{h^3} \quad (12)$$

Figure 2 shows the theoretical pressure profiles of CLIP and iCLIP (single injection) for net zero Stefan force at each slice for Newtonian and non-Newtonian resins. Theoretical Stefan force calculations for variable numbers of injection sites in a circular part cross-section are shown in Figures 2b-i for Newtonian and non-Newtonian resins respectively. Three approaches provide validation for our modeling. Besides analytical derivations, we perform three-dimensional simulations of the steady, incompressible Navier-Stokes equations using the SimpleFoam steady-state solver that is part of OpenFOAM, a flexible open source CFD package [33]. SimpleFoam uses the SIMPLE (Semi-Implicit Method for Pressure Linked Equations) algorithm [34] to solve the governing equations and boundary conditions, and we assume the flow is quasi-steady and laminar from the Stokes flow nature of the lubrication problem. We justify this assumption with the observation that the time for diffusion of momentum across the gap, $\tau_D=\frac{h^2}{v}$, where h is the deadzone gap thickness and v is kinematic viscosity, is much shorter than the time scale for the movement of the printed geometry, $\tau_G=\frac{h}{V}$, where V is the platform speed:

$$\frac{\tau_D}{\tau_G}=\frac{\frac{h^2}{v}}{\frac{h}{V}}=\epsilon\frac{hU}{v}=\epsilon Re\ll 1$$

where the Reynolds number, $Re = \frac{hU}{v}$, is the ratio of inertial forces to viscous forces, and $\epsilon = \frac{h}{L}$, where h is as before the deadzone gap thickness and L is the characteristic length of the part's cross-section.

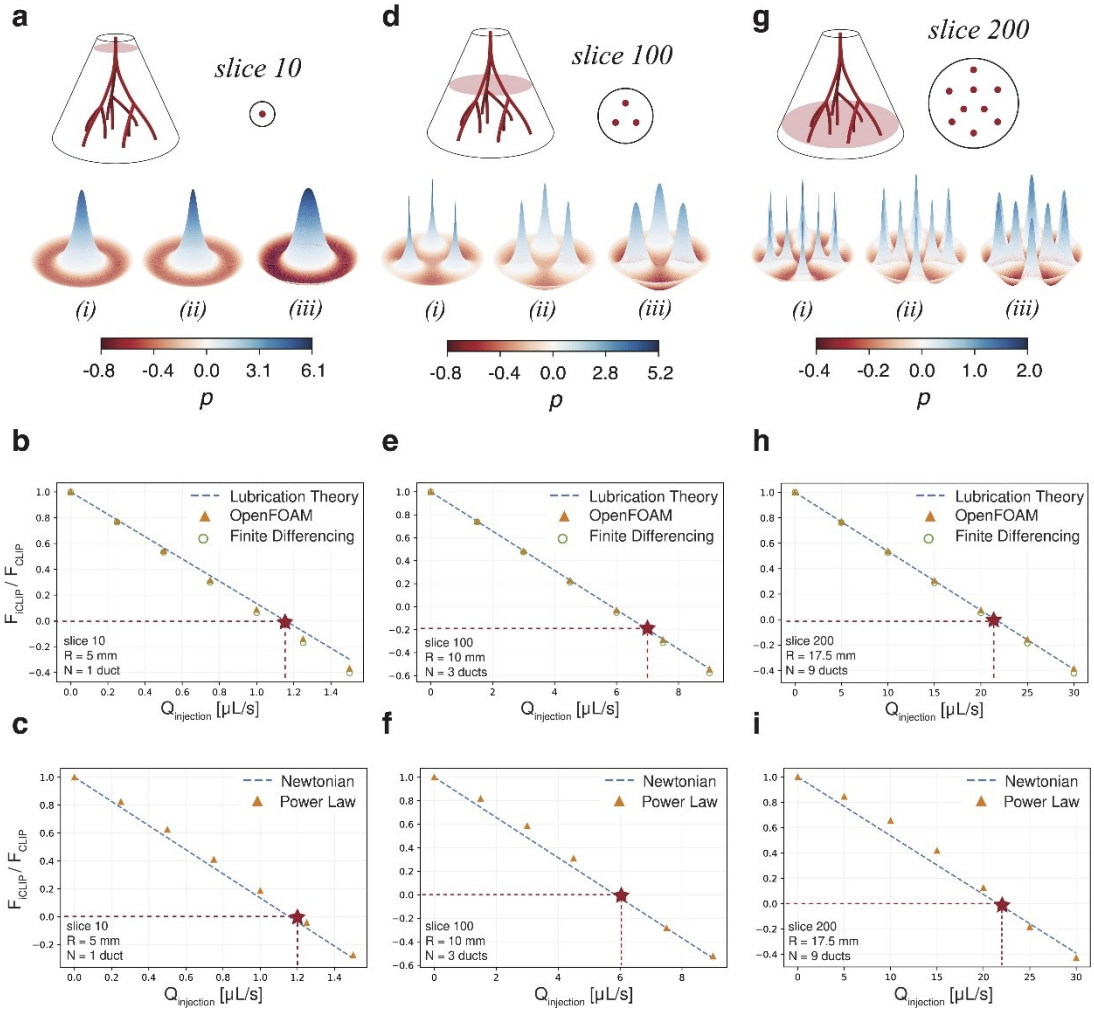

Figure 2. Theoretical modeling of iCLIP 3D printing with multichannel networks. Reduction in Stefan force with injection flow rate for a cone with a fluidic network (top) while printing with a Newtonian resin (middle) or non-Newtonian resin (n=0.4, bottom) for the cases of injecting through one **(a-c)**, three **(d-f)**, and nine **(g-i)** channels. Results shown for **(i)** lubrication theory, **(ii)** OpenFOAM, **(iii)** Finite differencing. Red dashed lines and stars indicate injection rate derived to be necessary to fully offset suction.

Thus, the steady three-dimensional Navier-Stokes equations are solved using no-slip boundary conditions on the fixed bottom plate and on the moving top stage. A fully developed Hagen–Poiseuille velocity profile is used for the velocity boundary condition at the injection ports in the case of a Newtonian resin. For a shear-thinning resin (approximated using a power-law viscosity model, see Equation 12), a plug flow velocity profile is used instead at the injection ports. A homogeneous pressure boundary condition is imposed on the sides of the cylindrical computational domain where the fluid is drawn from the resin bath. We use a computationally efficient fine, structured hexahedral mesh for the thin fluid domain. Computer simulations were performed making use of 32 compute cores on a single node per run. Finally, within the lubrication approximation, a third method was employed that is particularly

important for Newtonian flow in geometries with irregular cross sections. In this method, we solve Poisson's equation in 2D with finite differencing. All methods suggest that higher part cross sections demand higher injection rates including through an increased number of injection sites to offset Stefan adhesion. These calculations thus provide an operating injection rate required to fully offset suction, guiding our computational fabrication approach described below in Section 3.

3. Materials and methods

3.1. Hardware

Print platform motion was driven by a Nema 57 stepper motor supplied by a 12-V power bank. The UV light engine, with a total projection area of 76.8 mm by 48 mm, had a 3DLP9000 (Digital Light Innovations, TX, USA) with a 4-million-pixel 2560 × 1600 digital micromirror device (DMD), a 385-nm light-emitting diode (LED) and a 30-um field-of-view projection lens, using a DMD chip set (DLP9000, Texas Instrument, TX) with a projection lens (385-nm UV wavelength, 2560 × 1600 DMD array), 7.6-um by 7.6-um pixel size, and build area of 19.5 mm by 12.2 mm. Printer coordination was through an Arduino microcontroller with Marlin firmware.

While we employ a custom-built printer for taking load cell measurements, we also evaluate our injection scheme on a commercial printer, for closest comparison with state-of-the-art CLIP-based printing. For these experiments, we utilize an M1 printer from Carbon3D with four holes in the platform. The minimum positive feature resolution of this printer is advertised to be 75 microns in the x and y directions, and a maximum of 200 microns in the z direction. For custom printing, traditional printer hardware elements, namely the build platform and light projector, can be coordinated with the add-on syringe pump. We used a Harvard Apparatus PHD Ultra syringe pump with a maximum linear force of 75 lbs. Our own custom user interface allows the designer to adjust resin flow during printing as desired.

3.1.1 Optical coherence tomography

We use optical coherence tomography (OCT) [35] to visualize flow in CLIP and iCLIP. We in particular utilize a Ganymede Spectral Domain system (GAN621) from Thorlabs (Thorlabs, Newton, NJ, USA), with a center wavelength of 900 nm, a resolution of 3 microns, an imaging depth of 1.9 mm, and an A-scan line rate of 5 to 248 kHz, supplementing our resin with silica nanoparticles (Silicon Dioxide SiO2 Powder, US Research Nanomaterials, 0.90 g/cm3, ~400 nm particle size).

3.1.2 Load cell measurements

The build platform was tailored to fit the Miniature S-Beam Jr. Load Cell 2.0 (Futek, Irvine, CA, USA), which has dimensions of 1.9 cm by 1.75 cm by 0.66 cm. This load cell offers a resolution of ±0.05 %, a rated output ranging from 1 mV/V (250 g) to 2 mV/V (0.453 to 45.3 kg), and a 2000 cycles/s bandwidth. Additionally, a USB Load Cell Digital Amplifier from Futek was used for signal processing. During the printing process, force data measurements were captured at a frequency of 100 Hz. Notably, these measurements were taken midway through printing, at the point when the build platform had fully risen from the resin vat, ensuring stable buoyancy forces between layers. We performed calibration of our load cell before every print in order to offset both the effect of gravity and, more importantly, the effects of

buoyancy on the overall measured Stefan force by the load cell. We note that, as discussed in detail below, many factors affect the resulting sensor measurements, including but not limited to the viscosity of the resin used, the platform speed, and the interlayer delay time.

3.1.3 Print scripting

We tune platform speed by custom print scripting, modifying pump motion, platform velocity, and delay time. Stage velocities were between 500 mm/hr and 5000 mm/hr, layer thicknesses were 100 μm, and UV exposure times were 3.5 s. In all experimental comparisons between our approach and state-of-the-art, print parameters were held constant. We quantified the position of failure by the onset of either stair-stepping or delamination of objects from the platform. To quantify maximum unsupported overhang and required support, we generate supports utilizing a commercially-available generator from Carbon3D [15], or fluidic networks utilizing our custom design tool described in Section 3.3.

3.2. Materials

3.2.1 Photopolymer resins and rheological characterization

For UV curable materials, we used commercially available rigid thermosets, in particular white urethane methacrylate 90 (UMA 90) marketed as an inexpensive prototyping rigid resin from Carbon3D, Inc. [15], along with elastomeric polyurethane (EPU 40) also from [15] and a commercial elastomer resin, namely Formlabs Elastic 50A. Rheological characterization was carried out on uncured resin blends using an ARES rheometer [TA Instruments, Sesto San Giovanni (Mi), Italy]. A 25-mm parallel plate configuration was used with 0.1-mm gap between plates. Tests were carried out with the temperature set to 20°C, with shear rate range starting at 1 inverse seconds. Viscosities were then determined by the mean apparent viscosity at shear rates between 10 and 30 inverse seconds. Apparent viscosity was taken as the average stress/shear ratio between shear rates of 1 and 10 inverse seconds.

3.3. Inverse design algorithm

We utilize our custom inverse design algorithm to evaluate our approach in reducing the need for support structures, building on the basic algorithm introduced in prior work [36]. However, for the highly complex and irregular geometries considered in this work, along with the multichannel design and fabrication developed in this work, computational efficiency is critical, as is validation by multiple simulation methods and real- world experimental data. First, to accelerate computation time, we derive an adaptive slicing algorithm. Slices with shallower overhangs are at higher risk of suction-related failure due to "wobble" instabilities (Figure 4), whereby the growing object rotates during printing, and hence we adaptively sample these slices for our network control point placement. For such control point placement, we subdivide the part footprint into Voronoi tesselations and implement a particle swarm optimization routine as an evolutionary algorithm. To produce a network within the part, we subtract the network from model 2D image binary slices. Our multichannel design for additive manufacturing framework is summarized in Figure 3.

The design objective is to construct a fluidic network that can facilitate resin flow to nullify suction at every layer during printing. This design can be represented as a graph $G \equiv (N, E)$ with nodes $N =$

$\{n_i\}$ subject to certain fabrication process constraints. First, all the nodes of the network graph G must be linked and connected to the root note n_0. Second, the fluidic network must be fully closed. Third, the network is monotonically increasing with respect to the printing direction. Finally, channel radii must exceed the minimum negative feature resolution of the printer.

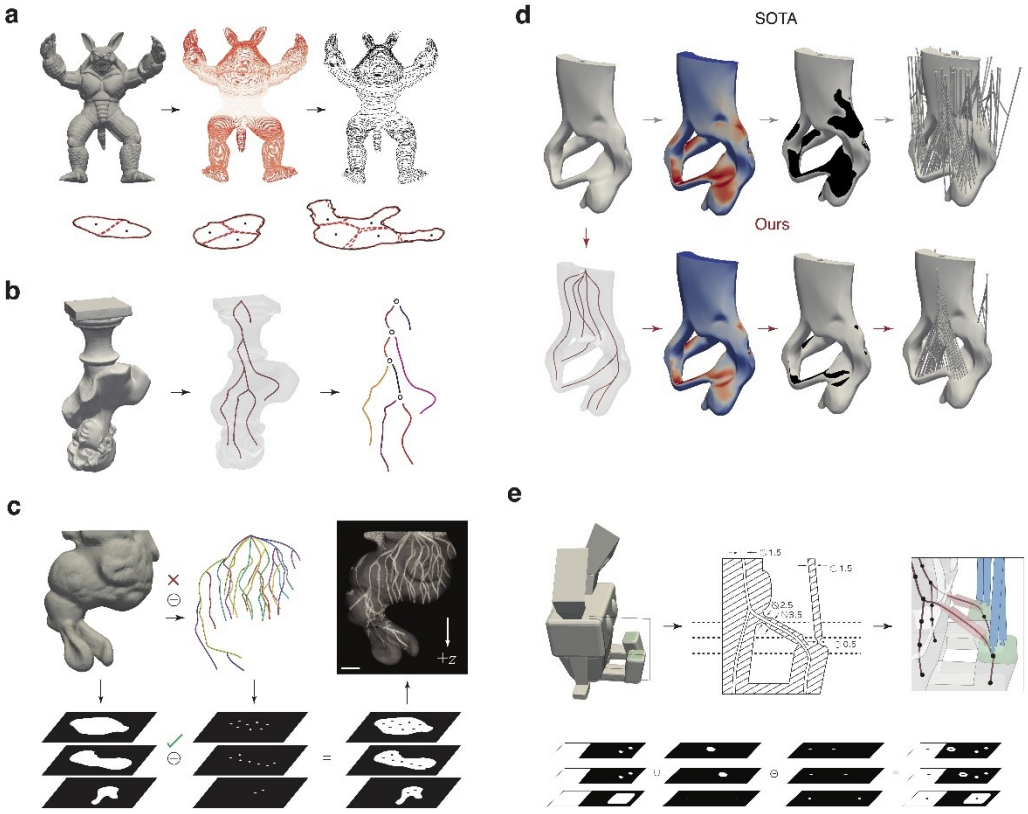

Figure 3. Multichannel inverse design approach. **(a)** Custom adaptive slicing algorithm with geometry tesselation for network control point placement, where for this Armadillo model red indicates interlayer intersections and grey slices to subsequently analyze. **(b-c)** Avoidance of 3D Boolean operations on mesh geometry by independent Bezier curve sweeping **(b)** and multichannel set generation based on bifurcation points **(c)**. **(d)** Method of integration with support structure generators. **(e)** Method of external channel swept pipe integration.

Our approach begins a network with an input injection node, thereafter positioning new nodes at optimal positions, as determined by our deadzone pressure modeling, to offset suction during printing. The input syringe pump injection rate is increased every time the network is extended with a new branch, increasing the cumulative flow. Branches may either contain outlets or not, hence not contributing to flow. Our approach also integrates an evolutionary module [37]. The final network is used to produce a series of smooth NURBS curves, swept into a mesh 3D geometry. To predict flow from a single input flow rate q_{in} to all outlet nodes $\{n\}_l$ in layer l with varying outflows $q_{out}(n)$, we model G as an electrical circuit [38], such that if a branch b terminus is solidified within the object, it does not add to circuit outflow. In our evolving graph G, this is described by the case when a parent node n in layer l is assigned no child nodes in layer $l+1$, such that node n is a leaf node and the corresponding branch b terminates. In this case, input injection flow q_{in} is redirected to remaining active branches.

Combined with our forward fluid dynamics model, which predicts pressure profiles p and

corresponding suction forces F_s for a given layer l with regions S and a distribution of nodes n and given flow rates from every node $q_{out}(n)$, this allows us to compute a predicted pressure profile using a vector of potentially varying outflows q_{out} for a given input flow rate q_{in}. Each time a node n is added to a layer l, the input injection rate q_{in} is incremented. We repeat until our termination criterion of zero net fluid suction is satisfied, *i.e.* $F_s = 0$ at any section S, or formally:

$$n_l, q_{in}(l) \rightarrow \{|F_s(S)| \leq 0 \; \forall \; S \in L\} \tag{13}$$

This produces a time-dependent syringe pump injection profile $q_{in}(l)$, which can be sent as serial commands over the course of the entire print. Layers l of the part Pcontaining footprints S with larger cross sectional areas require more injection sites $\{n\}_l$ and, correspondingly, higher input injection rates q_{in} to fully offset suction forces F_s. Having generated an initial network G offsetting suction forces F_s in all 2D cross sections $S$of 3D part P, we subsequently perform a metaheuristic evolutionary optimization routine to minimize the magnitude of $pmin$ in all layers l. Specifically, we implement a genetic algorithm where a candidate solution $\{n\}$ is described by the position of one, or multiple, injection nodes n, and an optimal solution $\{n\}_{opt}$ is that which minimizes $|p_{min}|$. To calculate the location x of minimum fluid pressure p_{min} for a given part cross section S, it is not necessary to solve for the full fluid pressure distribution $p(\mathrm{x})$ every iteration that positions of nodes $\{n\}$ are updated, which would be computationally expensive. Rather, $p_{min}(\mathrm{x})$ will be located at the point x in S with the greatest Euclidean distance $d(\mathrm{x})$ to either the part contour Ω or an injection node n:

$$d(\mathrm{x}) = min\{\|\mathrm{x} - n\|_2 \; \forall \; n \in \mathbf{n}, \|\mathrm{x} - \Omega\|_2\} \tag{14}$$

This subdivides S into a number of Voronoi regions [39] equal to $|\mathbf{n}| + 1$ for part cross section S, each specified either by one of $|\mathbf{n}|$ injection nodes in S containing all points closest to node n:

$$V(n_i) = \{\mathrm{x} : d(\mathrm{x}, n_i) \leq \mathrm{d}(\mathrm{x}, n') \; \forall \; n' \; \in \mathrm{N}\} \tag{15}$$

or by the part contour Ω supplying fluid via suction and all points closer to Ω than to any node n:

$$V(\Omega) = \{\mathrm{x} : d(\mathrm{x}, \Omega) \leq d(\mathrm{x}, n') \; \forall \; n' \; \in \mathrm{N}\} \tag{16}$$

The final network G representing the fluidic system as a fully connected graph is used to form to a series of NURBS curves. This parametric CAD is swept to produce a positive network 3D geometry, and finally Boolean differenced with the original B-rep CAD model via surface-to-surface intersection [40] to produce negative channels, hence an innervated part P'. While there is one optimal network that minimizes $|p_{min}|$, many feasible network configurations may both offset suction F_s, for all layers l, while satisfying the design space constraints described above. Formally the solution set of potential networks G with a fluid pressure threshold p_{min} is described by:

$$\{G\} = \{G \rightarrow \forall \; \mathrm{x} \in \mathrm{P}, \; p(\mathrm{x}) > p_{min}\} \tag{17}$$

with an optimum that minimizes suction forceF_s:

$$G_{opt} = \underset{G \in \{G\}}{\operatorname{argmin}} \sum_l F_s \, (l) \tag{18}$$

More details concerning our inverse design approach can be found in Supplementary Algorithm 1.

4. Experimental evaluation

4.1. In situ validation

We demonstrate accurate modeling of suction forces and control of suction by injecting through a varying number of channels. As shown in Figure 4, printing a single layer without injection is accompanied by a positive (*i.e.* tensile) force on the platform, reflective of suction forces on the part during traditional CLIP. This is corroborated with our flow visualizations in Supplementary Video 1, which show window drumming every layer of traditional printing. Moreover, the peak of this Stefan force is directly correlated with parameters such as part cross section and print speed, as expected from our theoretical modeling in Section 2. For the case of cone, square, and cylindrical geometries, increasing print footprint corresponds with higher measured Stefan forces, as quantified in more detail in Figure S6; moreover, as also expected from theory, this load cell can illustrate the viscosity-dependence of this force: significantly higher Stefan forces while printing the same cylindrical geometry with a high viscosity resin than a low viscosity one were measured. This was found for a wide range of parameter variations, and multiparameter sweeps, for resins of varying viscosity, and with parts containing different primitive cross-sectional geometries. While an overall positive correlation is observed for (i) part cross sectional area, (ii) resin viscosity, and (iii) print speed with Stefan force, the quantitative degree to which such parameters affect the suction force on the part have significant implications for the success or failure of a print, justifying both our analysis in Section 2 and our variable injection schemes to partially or fully offset such suction, as discussed below.

We thereafter validate the impact of one and multiple injection channels in alleviating these suction forces. Both force sensors and OCT *in situ* scanning provide experimental validation of our injection scheme. Injection causes a counteracting compressive force, proportional to the number of injection sites as expected from Equations 5-4b, and as visualized in Supplementary Video 2. We image flow through a single channel in such a network in Figure 4c, where infusion into the deadzone and out of the part periphery is apparent. We observe that for relatively small area parts, continuous infusion of resin through a single channel running through the axisymmetric center of a cylindrical part is sufficient to nearly nullify suction. We find that integrating not one, but multiple channels within the part, further reduces the Stefan force. For two simple primitive geometries, cones and squares, such results are shown in Figure 4d-e, respectively.

We show such multichannel networks significantly improve print results. Characteristic defects observed in unsupported geometries printed with the traditional method are illustrated in Figure 4f, including both stair-stepping and lip defects. Figure 4g shows an illustrative fluidic network in a cone geometry with channel radii of 500 microns. One channel aligned with the build platform port divides into three and then nine. For visualization, resin was removed from channels after printing, but typically channels are solidified leaving a solid part. Except for injection through this fluidic network, machine parameters were held constant.

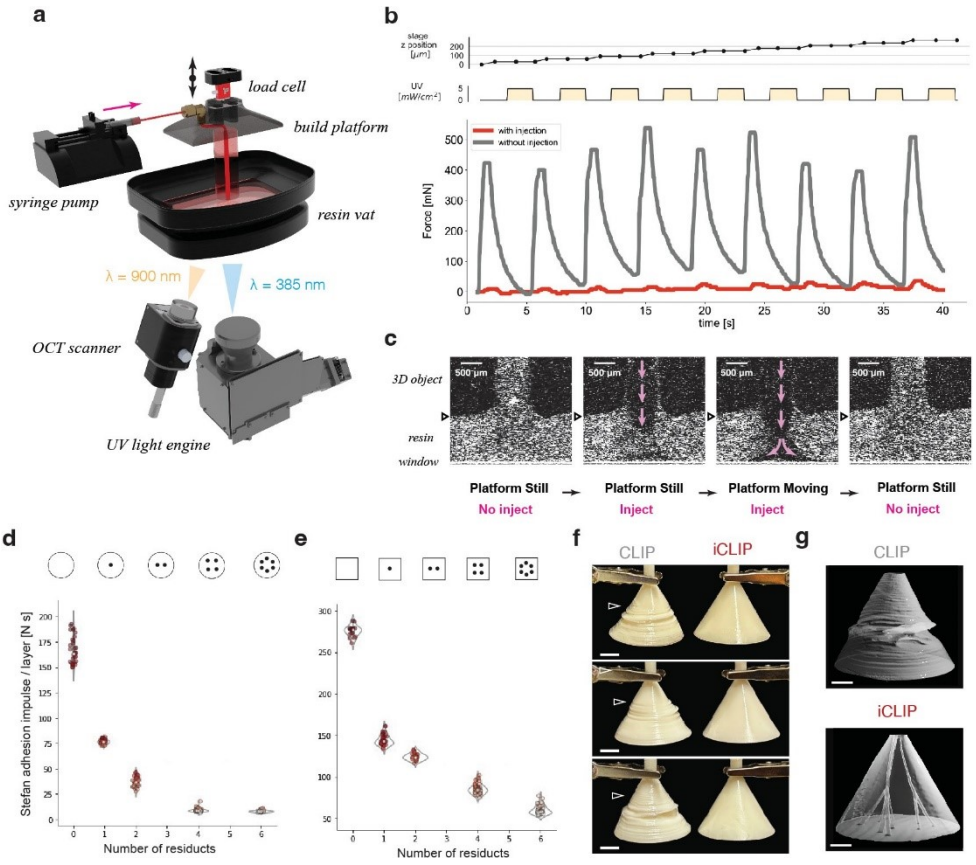

Figure 4. Multimodal experimental validation of suction offset by injection 3D printing. **(a)** *In situ* print measurement set-up. For a single embedded channel, **(b)** force measurement readings while not injecting (grey) and continuously injecting at 8 microliters/second (red) and **(c)** microscopic view of channel and deadzone via OCT scanning, with full videos of printing with and without injection included as Supplementary Videos 1-2. For multichannel networks, **(d)-(e)** dependence of Stefan force on number of embedded channels for two primitive geometries, **(f)** print results compared with no injection case, all other print parameters held constant. **(g)** µCT scans, all other print parameters held constant. Scale bar indicates 5 mm.

4.2. Experimental prints with primitive geometries

We first assess the performance of our approach compared with state-of-the-art continuous liquid interface production printing, for both geometric primitives considered in Section 2, *i.e.* cone and rod geometries. As shown in Figure 5, while with significant supports the traditional method can print steep overhangs, as expected, this leaves undesirable surface finish blemishes. If printed with fewer supports, however, layering defects manifest as lips and stair-stepping, worsened without supports entirely. While the print layer when such defects occur varies, they ensue at roughly similar locations once the cross-sectional area of the object grows beyond a critical point, as shown in Figure 5b-c. Specifically, a threshold angle of 30 degrees is observed before supports are needed to prevent "wobble" instabilities.

We quantify the maximum overhang by our method for both the rod and cone geometries. Qualitative results are shown in Figure 5d, where all print parameters except injection were kept constant, including print speed, layer thickness, and dark time between layers. We observe that our approach

increases the unsupported threshold overhang before failure, preventing suction-related layering defects and enabling better surface finish due to the obviation of supports. Figure 5e quantifies these maximum achievable unsupported overhangs. We find that both both overhang angle and extent determines overhang printability, as expected from our theoretical modeling in Section 2. While the traditional method can print overhang angles less than 30 degrees unsupported, above this threshold defects occur. By contrast, we find our method can achieve unsupported overhangs of between 45 and 50 degrees before failure, at which point we observe layering defects as in the traditional process at 30 degrees. Additional confirmation results for the rod geometry are shown in Figure S7.

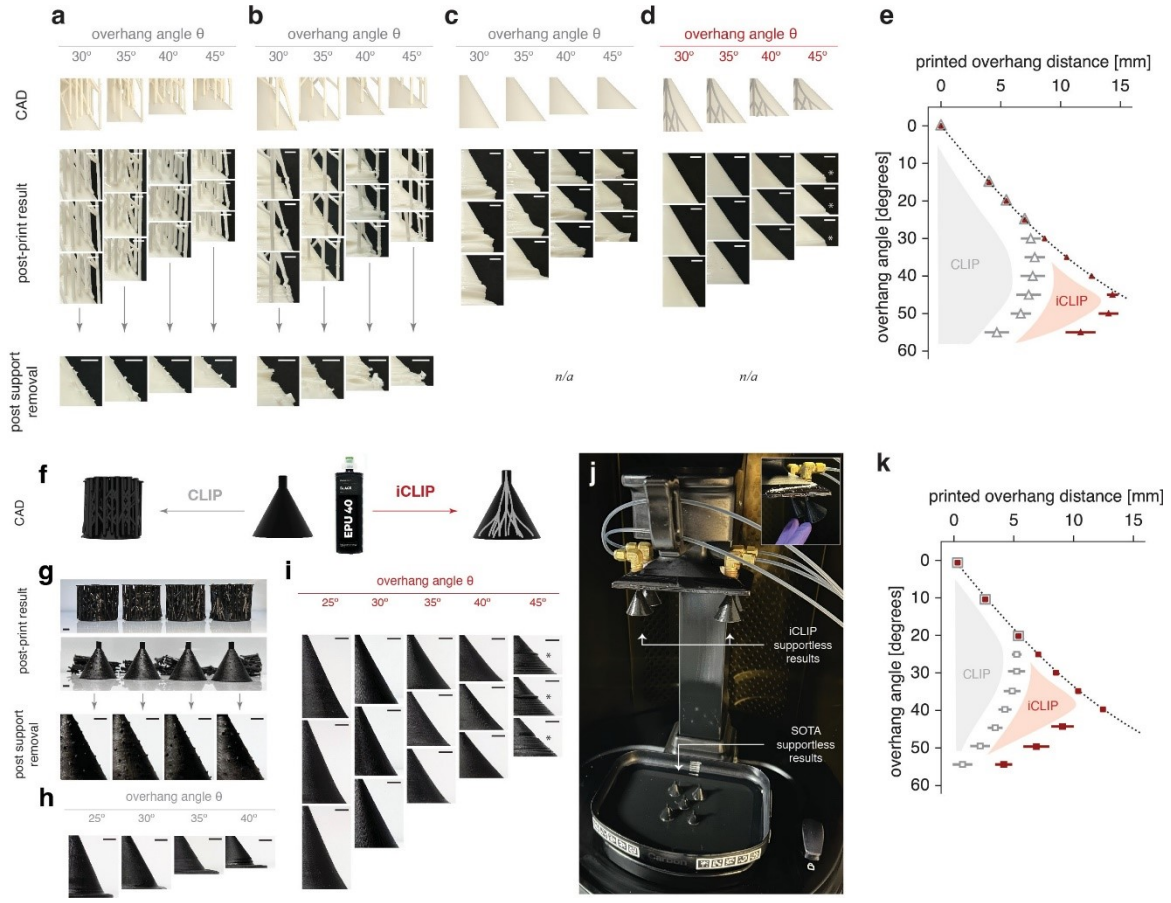

Figure 5. Experimental validation of our approach with primitive geometries. (a-e) Rigid resin print results. **(a)** Results for varying overhang angles by state-of-the-art with recommended supports **(a)**, SOTA with half recommended supports **(b)**, SOTA without supports **(c)**, and our approach without supports **(d)**. Quantified achievable overhangs by SOTA and our approach for rigid resins. Error bars denoting +/- one standard deviation from mean of technical triplicates. White arrows denote suction-related defects. **(f-k)** Elastomeric resin print results. **(f)** Printing with elastomeric resin by SOTA requires significant supports by industry software to ensure printability but leave behind surface defects **(g)**; without them, suction-related defects ensue **(h)**. With our approach, elastomers can be printed supportless at farther overhangs without defect **(i)**. **(j)** shows results from the same print job with both methods, with four iCLIP prints successfully completed and five CLIP prints delaminated in center. Results are quantified in **(k)**. Scale bars indicate 5 mm throughout.

As discussed in Section 1, the most challenging resins to print, but also among the most attractive for numerous applications, are elastomers. We summarize these additional support requirements printing with elastomer imposes on a print job in Figure S8, where we use default settings on a commercial software [15] with the cone model to-be-printed in EPU40 elastomer, whose rheology was characterized above. Compared with rigid UMA 90, the volume of support required to print an identical conical geometry with this material is an order of magnitude higher. We then experimentally test the support requirements for printing by state-of-the-art with this material and by our method with the same material. CAD models indicating support requirements for CLIP are shown in Figure 5, where in agreement with the quantitative indications in Figure S8, the quantity of supports necessitated by the traditional process is even more significant than for rigid materials. While we observe such supports can indeed ensure printability, as shown in Figure 5, these leave behind irrecoverable surface defects, waste significant material, and require significant manual effort. We also observe, as shown in Figure 5, that when such supports are not included during printing by the traditional method (without injection), delamination of the elastomeric part from the platform ensues, *i.e.* print failure, for the case of all five negative controls included.

We observe similar results when printing the same primitive geometries with elastomeric resins via our iCLIP process and the traditional CLIP process. The results are shown in Figure 5f-k. The critical overhang threshold for the traditional approach, without injection, is slightly lower than for the case of the rigid resin, but once again, engineering a fluidic network within the part extends this maximum unsupported overhang significantly without layering or delamination failure. We perform the same experiment with injection through our co-designed fluidic networks; prints were run on the same platform and in the same print job as for the traditional cases, and hence by definition with the same print parameters, save for injection through the embedded bifurcating network, as shown in Figure 5. For the case with injection, no delamination occurs, despite the omission of surrounding scaffolding. This indicates elastomeric parts can be printed supportless thanks to our method; the resulting smooth surface finishes lacking surface defects from support cleavage are shown in Figure 5.

4.3. Experimental prints with complex geometries

To test our approach on geometric features characteristic of real-world 3D printing, we also evaluate our method on a sample of complex geometries. Specifically, we validate these results with several real-world prints sampled from the Thingi10k online repository [41]. Figure 6a-b shows these experiments, which are also shown in Supplementary Video 5, indicating timestamps and image slices projected during printing indicating supports, which are also shown in Supplementary Videos 6-7. Our approach prints these models 42% faster than state-of-the-art operating conditions, and with 70-75% fewer supports, without defect. Figure 6c shows further experimental validation on complex models; supports are still required by our method in some cases, as some regions exceed our method's maximum achievable overhang. The volumetric throughput is calculated by multiplying linear print speed in mm/hr by the area of the printed part in mm^2, not including support. Our method increases print throughput not just by increasing linear print speed: while the bridge geometry is printable by the traditional method with supports, this limits throughput to two parts per platform. Removing the need for supports frees platform surface for an additional two prints in this case. In addition to printing these test geometries unsupported, we also demonstrate our approach can print more quickly than state-of-the-art.

Pumping motions add significant delay time to the state-of-the-art process, which can be seen in Supplementary Video 3 and are empirically found to be needed to promote resin reflow and alleviate suction forces [15]. As shown in Supplementary Video 3, our method prints the same model in less than one hour, obviating pumping motions and increasing motor up-speed, which without injection increases Stefan forces as described in Equation 23.

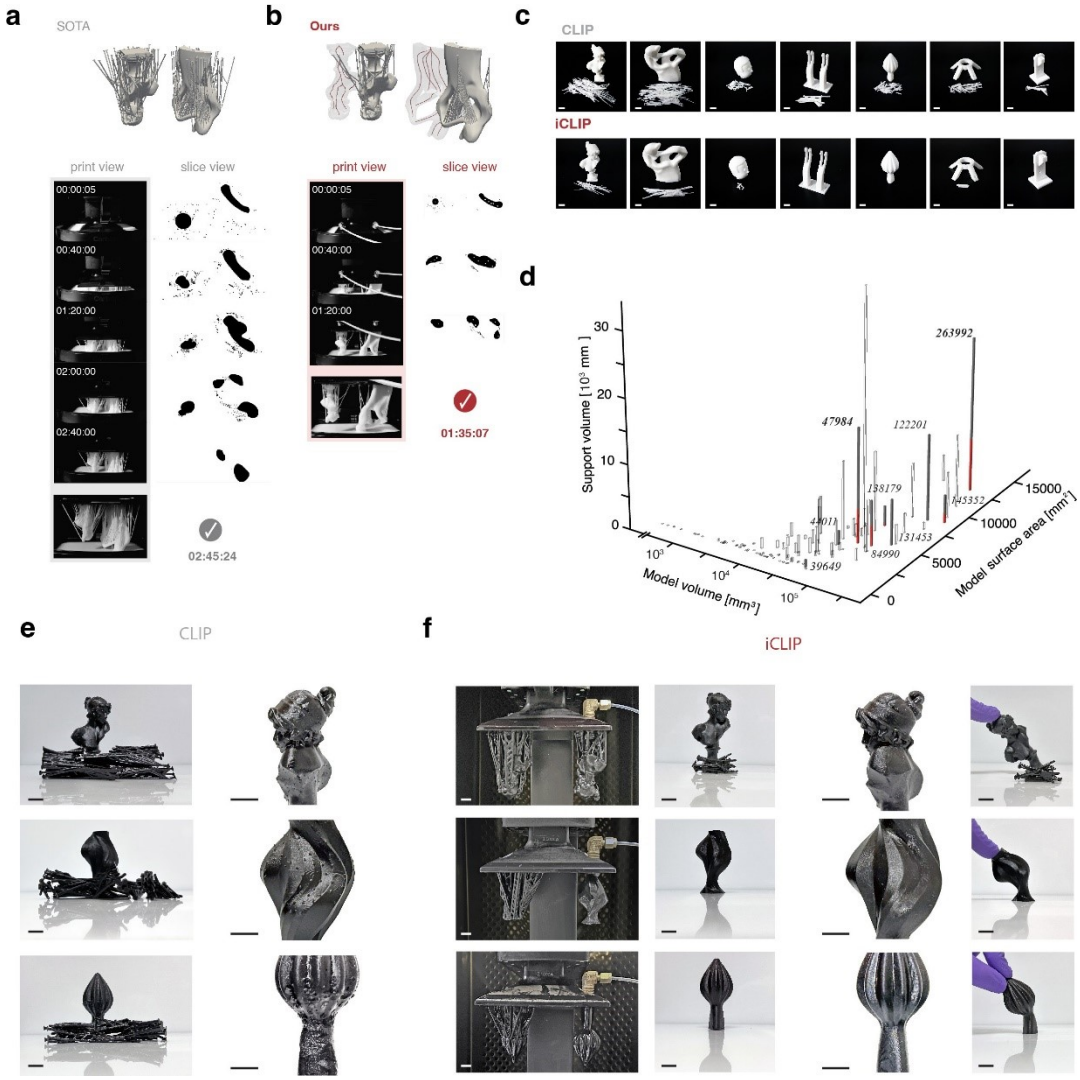

Figure 6. Experimental validation of our approach with complex geometries. **(a)** With rigid resin by state-of-the-art, with supports and time stamps indicated. **(b)** By our approach, with supports and time stamps indicated. **(c)** Support materials after printing for both methods. **(d)** *In silico* study predicting supports necessitated for a sample of Thingi10k CAD models. Models experimentally validated with real-world prints in this work are highlighted. For a series of three test models also from Thingi10k, results with elastomer resin by state-of-the-art **(e)** and our approach **(f)**, with supports indicated. Scale bars indicate 10 mm.

We quantify the potential benefits of our approach with an *in-silico* analysis in Figure 6, taking a random sample of Thingi10k 3D printed models and procedurally generating required support volumes for both approaches. This analysis suggests our method offers little advantage when printing small

volume models requiring little support to begin with. For large-volume prints, though, our method extends the maximum achievable unsupported overhang angle in a user's 3D model. We also validate our results with complex geometries with elastomeric resins, as shown in Figure 6e-f. As before, we demonstrate our approach can print models that would by state-of-the-art printing use significant supports, either supportless or with significantly less support. The impact of support cleavage on elastomer parts is even more noticeable than on rigid parts, as shown in Figure 6e, and is ameliorated when our approach can print without such scaffolds Figure 6f.

As mentioned above, the potential to 3D print with highly flexible materials is giving rise to numerous industrial applications. One such use case is in the area of soft robotics, where intricate geometry can now, in theory, be combined with deformable materials to achieve desired actuation performance [42]. Nonetheless, the adhesion-related fabrication challenges described in this work, including slow print speeds and exacerbated support requirements, among others, render 3D printing currently a relatively inefficient method to fabricate such soft robotic actuators. We demonstrate the advantages of our approach by simplifying the production of an example *Pneunet*, as shown in Figure S9, which achieves asymmetric deformation upon the application of pneumatic pressure at one end thanks to the combination of a strain limiting and extensible layer [43]. For this geometry, as for the case of the cone discussed previously, state-of-the-art methods stipulate high quantities of supports, at times exceeding 90 percent of the illuminated part cross section. As before, such supports do ensure printability by visibly providing structural stiffness to the green strength printed object; however, the challenges associated with removing such supports from the printed object, which is liable to tear in its green state, are particularly acute. We demonstrate that whereas the traditional approach requires significant support scaffolding, we are able to print this device unsupported. Second, we employ the same fluidic network used for injection for an automated post-cleaning step. We note that the typical post-processing step is to simply solidify the resin trapped within the channels, which is always the case as the resin is viscous and the channel diameters are relatively small. This is achieved using a post-UV or thermal cure step, which is standard practice for resin 3D printing generally.

5. Discussion and limitations

While we experimentally show our approach reduces the supports required for a user's 3D model, it cannot at present print unsupported overhangs exceedingly approximately 50 degrees, either symmetric or asymmetric, without defect. We observe this for both rigid, Newtonian resins and elastomeric, non-Newtonian resins. We explain this breakdown of our approach by noting that while injection may cumulatively offset suction, wobble and tilt instabilities may still be caused be remaining regions of low pressure that are difficult to completely offset. Moreover, "island" geometries, *i.e.* those without pre-existing cured polymer for attachment, still necessitate supports. Despite this, as discussed in Section 4.3, we argue that quantitatively extending this maximum overhang threshold presents the potential for significant material savings, particularly for large volume models. An important limitation of our method is the need to incorporate a channel into the final object, possibly not feasible for very small features. Another restriction is that, while offsetting Stefan forces, we do not solve the temperature limitation on the speed of resin 3D printing, which is exothermic. Fabricating large objects evolves large quantities of heat, posing dangers to printer hardware or causing part warping and ultimately putting an upper bound on our

method's print speeds. Future work will investigate the possibility of using cooled resin to remove this limitation.

In this work, we describe our simulation-based control strategy for CLIP and iCLIP-based 3D printing. We describe our lubrication theory-based approach to simulating the deadzone in both processes, for both single and multiple injection sites and for Newtonian and non-Newtonian resins. We further provide experimental validation, for both the case of single and multiple sources, of such theoretical modeling, demonstrating that injection in controlled fashion is able to tuneably reduce Stefan adhesion forces. We do so for both the case of a single injection port through the platform, and multiple such ports, along with on elastomeric resins with non-Newtonian rheology.

Acknowledgments

GEL is supported by a National Science Foundation Graduate Research Fellowship Program grant. This work was supported in part by the Stanford Precourt Institute for Energy and the Stanford Woods Institute for the Environment.

Conflicts of interest

J.M.D. declares that he has an equity stake in Carbon Inc., which is a venture-backed start-up company that owns related U.S. Patent 9,216,546, U.S. Patent 9,360,757, and others.

Authors' contribution

GEL and IAC performed experiments. GEL and NK performed mathematical modeling. ESGS, JMD, and GEL wrote and revised the manuscript.

Disclaim

Part of the data reported in this study has been presented at the conference ACM Symposium on Computational Fabrication (SCF) 2023 [44].

References

[1] Wohlers T, Campbell RI, Diegel O, Huff R, and Kowen. 3D Printing and Additive Manufacturing State of the Industry. *Wohlers Report* 2020.
[2] Zhao WY, Wang ZY, Zhang JP, Wang XP, Xu YT, et al. Vat photopolymerization 3d printing of advanced soft sensors and actuators: From architecture to function. *Adv. Mater. Technol.* 2021, 6(8):2001218.
[3] Zhakypov Z and Okamura AM. Fingerprint: A 3-d printed soft monolithic 4-degree-of-freedom fingertip haptic device with embedded actuation. In *2022 IEEE 5th International Conference on Soft Robotics (RoboSoft)* 2022, pp. 938–944.
[4] Surjadi JU, Zhou YS, Huang SP, Wang LQ, Li MY, et al. Lightweight, ultra-tough, 3d-architected hybrid carbon microlattices. *Matter* 2022, 5(11):4029–4046.
[5] Xu XY, Awad A, Robles-Martinez P, Gaisford S, Goyanes A, et al. Vat photopolymerization 3d printing for advanced drug delivery and medical device applications. *JCR* 2021, 329:743–757.
[6] Gurung A. Makers: The new industrial revolution. *CR* 2014.
[7] Jin J, Yang JF, Mao HC, and Chen Y. A vibration-assisted method to reduce separation force for

stereolithography. *J. Manuf. Process* 2018, 34:793–801.
[8] Li XJ, Mao HC, Pan YY, and Chen Y. Mask video projection-based stereolithography with continuous resin flow. *J. Manuf. Eng.* 2019, 141(8):081007.
[9] Song HT, Rodriguez NA, Seepersad CC, Crawford RH, Chen M, et al. Development of a variable tensioning system to reduce separation force in large scale stereolithography. *AM* 2021, 38:101816.
[10] Wang JC, Ruilova M, and Lin YH. The development of an active separation method for bottom-up stereolithography system. In *2017 IEEE/SICE International Symposium on System Integration (SII)* 2017, pp. 108–114.
[11] Tumbleston JR, Shirvanyants D, Ermoshkin N, Janusziewicz R, Johnson AR, et al. Continuous liquid interface production of 3d objects. *Science* 2015, 347(6228):1349–1352.
[12] Kowsari K, Zhang B, Panjwani S, Chen ZC, Hingorani H, et al. Photopolymer formulation to minimize feature size, surface roughness, and stair-stepping in digital light processing-based three-dimensional printing. *AM* 2018, 24:627–638.
[13] Tumbleston JR, Shirvanyants D, Ermoshkin N, Janusziewicz R, Johnson AR, et al. Continuous liquid interface production of 3d objects. *Science* 2015, 347(6228):1349–1352.
[14] Janusziewicz R, Tumbleston JR, Quintanilla AL, Mecham SJ, and DeSimone JM. Layerless fabrication with continuous liquid interface production. *PNAS* 2016, 113(42):11703–11708.
[15] Inc. Carbon. "carbon dls 3d printing process engineering handbook", June 24, 2022.
[16] Hsiao K, Lee BJ, Samuelsen T, Lipkowitz G, Kronenfeld JM, et al. Single-digit-micrometer-resolution continuous liquid interface production. *Sci. Adv.* 2022, 8(46): eabq2846.
[17] Cosmi F and Maso AD. Experimental characterization and validation by fem analyses of a 3d-printed support. In *IOP Conference Series: Materials Science and Engineering* 2021, 1038:012009.
[18] Giani N, Mazzocchetti L, Benelli T, Picchioni F, and Giorgini L. Towards sustainability in 3d printing of thermoplastic composites: Evaluation of recycled carbon fibers as reinforcing agent for fdm filament production and 3d printing. *Composites Part A: Applied Science and Manuf.* 2022, 159:107002.
[19] Hornus S, Lefebvre S, Dumas J, and Claux F. Tight printable enclosures and support structures for additive manufacturing. In *Proceedings of the Eurographics Workshop on Graphics for Digital Fabrication* 2016 pp. 11–21.
[20] Dumas J, Hergel J, and Lefebvre S. Bridging the gap: automated steady scaffoldings for 3d printing. *ACM Trans. Graph* 2014, 33(4):1–10.
[21] Schmidt R and Umetani N. Branching support structures for 3d printing. In *ACM SIGGRAPH 2014 Studio* 2014, pp. 1–1.
[22] Vanek J, Galicia JAG, and Benes B. Clever support: Efficient support structure generation for digital fabrication. In *Computer graphics forum* 2014, 33:117–125. Wiley Online Library.
[23] Keneth ES, Kamyshny A, Totaro M, Beccai L, and Magdassi S. 3d printing materials for soft robotics. *Adv. Mater.* 2021, 33(19):2003387.
[24] Everitt A, Eady AK, and Girouard A. Enabling multi-material 3d printing for designing and rapid prototyping of deformable and interactive wearables. In *20th International Conference on Mobile and Ubiquitous Multimedia* 2021, pp. 1–11.
[25] Bai H, Li S, and Shepherd RF. Elastomeric haptic devices for virtual and augmented reality. *Adv. Funct. Mater.* 2021, 31(39):2009364.
[26] Schmitz M, Steimle J, Huber J, Dezfuli N, and Mühlhäuser M. Flexibles: deformation-aware 3d-printed tangibles for capacitive touchscreens. In *Proceedings of the 2017 CHI Conference on Human Factors in Computing Systems* 2017, pp. 1001–1014.
[27] Hudson SE. Printing teddy bears: a technique for 3d printing of soft interactive objects. In *Proceedings of the SIGCHI Conference on Human Factors in Computing Systems* 2014, pp. 459–468.
[28] Peng HS, Mankoff J, Hudson SE, and McCann J. A layered fabric 3d printer for soft interactive objects. In *Proceedings of the 33rd Annual ACM Conference on Human Factors in Computing Systems* 2015, pp. 1789–1798.
[29] Moheimani R, Agarwal M, and Dalir H. 3d-printed flexible structures with embedded

deformation/displacement sensing for the creative industries. In *AIAA Scitech 2021 Forum* 2021, pp. 0534.
[30] Schmitz M, Khalilbeigi M, Balwierz M, Lissermann R, Mühlhäuser M, et al. Capricate: A fabrication pipeline to design and 3d print capacitive touch sensors for interactive objects. In *Proceedings of the 28th Annual ACM Symposium on User Interface Software & Technology* 2015, pp. 253–258.
[31] Lipkowitz G, Samuelsen T, Hsiao K, Lee B, Dulay M, et al. Injection continuous liquid interface production of 3d objects. *Sci. Adv.* 2022, 8.
[32] Stefan MJ. Versuch über die scheinbare adhäsion, sitzungsber. *Abt. II, Österr. Akad. Wiss. Math.-Naturwiss. Kl*, 1874, 69:713–721.
[33] Weller HG, Tabor G, Jasak H, and Fureby C. A tensorial approach to computational continuum mechanics using object-oriented techniques. *Computers in physics* 1998, 12(6):620–631.
[34] Patankar SV and Spalding DB. A calculation procedure for heat, mass and momentum transfer in three-dimensional parabolic flows. In *Numerical prediction of flow, heat transfer, turbulence and combustion* 1983, pp. 54–73.
[35] Aumann S, Donner S, Fischer J, and Müller F. Optical coherence tomography (oct): principle and technical realization. *High resolution imaging in microscopy and ophthalmology: new frontiers in biomedical optics* 2019, pp. 59–85.
[36] Lipkowitz G, Shaqfeh E, and Desimone J. Paraflow: A computational design tool for support-free multimaterial 3d printing. In *Extended Abstracts of the 2023 CHI Conference on Human Factors in Computing Systems* 2023, pp. 1–8.
[37] Lipkowitz G, Shaqfeh ESG, and DeSimone JM. Fluidics-informed fabrication: A novel co-design for additive manufacturing framework. In *International Conference on Human-Computer Interaction* 2023, pp. 454–466.
[38] Oh KW, Lee KS, Ahn B, and Furlani EP. Design of pressure-driven microfluidic networks using electric circuit analogy. *Lab on a Chip* 2021, 12(3):515–545.
[39] Du Q, Faber V, and Gunzburger M. Centroidal voronoi tessellations: Applications and algorithms. *SIAM review* 1999, 41(4):637–676.
[40] Sederberg TW, Anderson DC, and Goldman RN. Implicit representation of parametric curves and surfaces. *Computer Vision, Graphics, and Image Processing* 1984, 28(1):72–84.
[41] Zhou QN and Jacobson A. Thingi10k: A dataset of 10,000 3d-printing models. *arXiv preprint arXiv:1605.04797*, 2016.
[42] Wallin TJ, Pikul J, and Shepherd RF. 3d printing of soft robotic systems. *Nat. Rev. Mater.* 2018, 3(6):84–100.
[43] Gu GY, Wang D, Ge L, and Zhu XY. Analytical modeling and design of generalized pneu-net soft actuators with three- dimensional deformations. *Soft robotics* 2021, 8(4):462–477.
[44] Lipkowitz G, Krishna N, Coates I, Shaqfeh E, Desimone J. Printing atom-efficiently: faster fabrication of farther unsupported overhangs by fluid dynamics simulation. *Proceedings of the 8th ACM Symposium on Computational Fabrication*. 2023, pp.1–14.